J. Space Weather Space Clim. 2023, **13**, 9

https://doi.org/10.1051/swsc/2023009

JSWSC

Available online at:
www.swsc-journal.org

RESEARCH ARTICLE OPEN ACCESS

Polar particle flux distribution and its spatial extent

Olesya Yakovchuk* and Jan Maik Wissing

Institute of Physics, University of Rostock, Rostock 18051, Germany

Received 31 May 2022 / Accepted 18 March 2023

Abstract – *Context*: The main challenge in atmospheric ionisation modelling is that sparse measurements are used to derive a global precipitation pattern. Typically this requires intense interpolation or scaling of long-term average maps. In some regions however, the particle flux might be similar and a combination of these regions would not limit the results even though it would dramatically improve the spatial and temporal data coverage.
Aims: The paper intends to statistically analyse the particle flux distribution close to the geomagnetic poles labelled as Polar Particle Flux Distribution (PPFD) and identify similar distributions in neighbouring bins. Those bins are grouped and the size of the PPFD area is estimated. The benefit is that single measurements within the PPFD area should be able to represent the particle flux for the whole area at a given time.
Methods: We use spatially binned energetic particle flux distributions measured by POES and Metop spacecraft during 2001–2018 to identify a Kp-dependent area with a similar flux distribution as the one found close to the geomagnetic poles ($|magn.lat| > 86°$). First, the particle flux is mapped on a magnetic local time (MLT) vs. magnetic latitude grid. In the second step, the gridded data is split up according to Kp levels (forming the final bins). Third, the particle flux in every bin has been recalculated in order to replace zero-count rates with rates based on longer measurement periods which results in a more realistic low flux end of the particle distribution. Then the binned flux distributions are compared to the PPFD. A "Δ-test" indicates the similarity. A threshold for the Δ-test is defined using the standard deviation of Δ-test values inside the ($|magn.lat| > 86°$) area. Bins that meet the threshold are attributed as PPFD area.
Results: PPFDs and the corresponding PPFD areas have been determined for all investigated particle channels, covering an energy range of 154 eV–300 keV for electrons and 154 eV–2.5 MeV for protons. Concerning low energy channels a gradual flux increase with rising Kp has been identified. High energy channels show a combination of background population and solar particle event (SPE) population that adds up with increasing Kp. The size of the PPFD area depends on particle species, energy and geomagnetic disturbance, as well as MLT. The main findings are: a) There are small but characteristic hemispheric differences. b) Only above a certain energy threshold do the PPFD areas increase with particle energy. c) A clear enlargement with rising Kp is identified – with exceptions for very low Kp. d) The centre of the PPFD area is shifted towards midnight and moves with Kp. Asymmetries of the boundaries could be explained by auroral intensity. e) For low-energy particles the main restriction of the PPFD area seems to be the auroral precipitation.

Keywords: Particle precipitation / Polar cap / Atmospheric ionisation model / Particle flux distribution

1 Introduction

This section gives an overview of particle precipitation in the high-latitude polar ionosphere and shows which attempts have been made in order to characterise it. It will also state why none of the existing descriptions matches our needs for particle precipitation modelling.

Polar Cap (PC): In the PC, the magnetic field lines are generally assumed to be open and connected to the solar wind, whereas the field lines outside the PC are closed (except of the cusp) and map to the plasma sheet and the plasma sheet boundary layer in the magnetosphere. These two substantially different magnetic and plasma domains are separated by a polar cap boundary (e.g., Sergeev, 1990; Newell et al., 2009). Early spacecraft observations revealed a very simple precipitation pattern of solar energetic electrons in the PC: a plateau pattern with intense and nearly homogeneous flux with a sharp drop-off to lower latitudes (for high energies e.g. Evans & Stone, 1972; Sergeev et al., 1987; Newell et al., 2009) or a rapid transition to even more intense auroral oval precipitation (e.g. Fig. 1 in

*Corresponding author: olesya@ionization.de

Wissing et al., 2008; Evans & Greer, 2006). It should be noted that Scholer (1972) found a factor 2 variation in flux measurements within a singular central polar cap crossing, concluding that it might be a time-delayed effect due to a magnetic discontinuity in the IMF that reconnects with deeper layers of the tail as it propagates outward. PC dynamics and associated particle precipitation are a reflection of different magnetospheric processes, such as the Dungey Cycle (Dungey, 1961; Milan et al., 2003) which leads to a day-night asymmetry in the precipitation pattern. In the substorm cycle, contraction and expansion of PC take place (Meng & Makita, 1986). Given its dependence on B_y it shows an additional asymmetry in the dusk-dawn direction (Lukianova & Kozlovsky, 2011). PC dynamics become even more complicated during geomagnetic storms (McEwen, 1998). It is important to note that particle precipitation is not always a good indicator of the PC. High energy particles originating from the interplanetary medium, in particular protons, may also precipitate outside the PC and thus partly overlap with auroral precipitation.

Polar Rain: The polar rain describes the precipitation of electrons (of a few hundred eV) originating from the solar corona (Winningham & Heikkila, 1974; Newell et al., 2009). As such the spatially homogeneous polar rain is used as an indicator for open field lines (Shirai et al., 1998). The orientation of the interplanetary field can cause hemispheric differences (Yeager & Frank, 1976).

Solar Energetic Particle (SEP) plateau region: The SEP plateau region indicates the area of intense and mostly homogeneous solar particle flux. While this region may coincide with the PC at the low geomagnetic disturbance and for lower particle energies, there may be significant differences during other conditions. Theoretically, it has been shown by Smart et al. (1969) that high-energy protons (as well as electrons) from outside the magnetosphere may reach lower latitudes than their low-energy equivalent. Additionally, there is a clear local time asymmetry in the cutoff rigidities. The energy dependence of the low latitude boundary can be seen e.g. in Figure 1 of Bornebusch et al. (2010). For a single orbit, the SEP plateau region borders can be determined (Feldstein & Starkov, 1967). Statistical analysis as by Bikkuzina et al. (1998) might be used to define the corresponding area. Consequently, the SEP plateau region depends on particle species and energy. For very high energies of the galactic cosmic rays even the term cut-off latitudes has been introduced (see e.g. Herbst et al., 2013).

Auroral Oval (AO) boundaries: The poleward boundary of the AO is of interest for the high-latitude polar ionosphere as it locates the occurrence of an auroral particle population. The AO boundaries are determined with radars (e.g. Chisham et al., 2004; Aikio et al., 2006), ground-based optical photometers (e.g. Blanchard et al., 1995; Johnsen et al., 2012), or magnetometers (e.g. Gary et al., 1998), but these methods have some limitations and are not favoured Lukianova & Kozlovsky (2013). The most popular approach to define the AO boundaries are satellite observations. Here it is possible to distinguish two main streams: a) optical measurements of auroral emission (e.g. Murphree et al., 1991; Lukianova & Kozlovsky, 2013) and b) in-situ particle measurements (e.g. Hardy et al., 1985; Newell et al., 2009). The identification of AO boundaries using the spectra of precipitating particles is considered the most reliable method (e.g. Gussenhoven & Brautigam, 1994; Sotirelis et al., 2005). Sometimes a) and b) are even used in combination (e.g. Kauristie et al., 1999; Baker et al., 2000). Satellite observations help to better understand the correlation between AO boundaries and geomagnetic activity (e.g. Craven & Frank, 1987; Milan et al., 2003; Carbary, 2005). While b) is direct information about the precipitating fluxes, it lacks spatial information. Thus several orbits have to be combined somehow in order to get a global picture. The optical measurements in a) return spatial information, but only represent a proxy without spectral information.

The problem with all these definitions is that they describe (e.g. the spatial pattern) of single particle sources. For example the location of polar rain, the spatial extent of SEPs or the location of auroral precipitation. However, when modelling particle precipitation and atmospheric ionisation the problem is more the other way around. Based on sparse measurements of a combined particle spectrum of different sources we need to know where these energy-dependent fluxes can be applied. And this area should also be clearly predefined and not determined on an event basis, as the satellite coverage may be limited (e.g. not enough passes to estimate the SPE region).

Therefore, we decided to compare the (long-term) particle flux spectrum in order to define an area with similar flux characteristics as measured at the geomagnetic poles.

2 Data sets

Precipitating fluxes are observed by several satellites, placed in low-altitude polar orbits. These are in-situ measurements along the path of the satellite. We used a long-term data set from the Polar Orbiting Environmental Satellites (POES) during 18 years (2001–2018) in combination with different levels of geomagnetic activity and the Magnetic Apex coordinate system. We also had to recalculate the particle flux as it contains high fractions of zero counts that do not allow a good statistical analysis. This section describes the data sets and how the data has been processed.

2.1 Particle data

Time profiles of 16 s averaged electron fluxes ranging from 0.15 to 300 keV and protons from 0.15 to 2500 keV measured on board the polar orbiting NOAA/POES and their successor, the Metop satellites (Evans & Greer, 2006), have been used for the period 2001–2018. The 16 s averages have always been derived from 2 s native satellite resolution using the binary format before 2014 and the netCDF format afterwards. All available data from POES 15, 16, 17, 18, 19 and Metop 01 and 02 have been included, except for POES 16 after 2006 as it is known that the TED data is erroneous (Evans, 2008).

The POES satellites have Sun-synchronous orbits at altitudes of ≈820 km (with ≈100-minute periods of revolution) and an inclination of ≈98.5°. The satellites have initially been placed in orbits that should cross the equator at a fixed local time either being morning-evening or day-night sector. However, these orbits were drifting slightly with time, allowing us to investigate the effect of local time on particle fluxes.

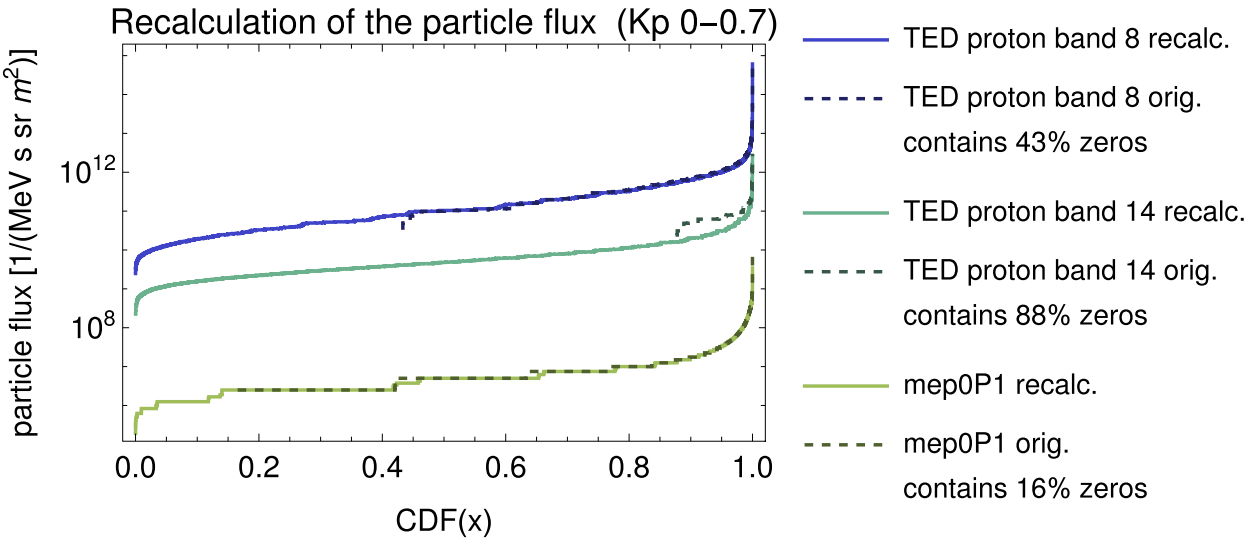

Figure 1. Original particle flux as given by the satellites is plotted against the recalculated flux. The cumulated distribution function (CDF, see *x*-axis) represents the probability that a specific particle flux (or less) appears.

Information about the different energy channels can be found in Table 1. All figures in this paper are given in differential particle flux in 1/(MeV m^2 s sr). The differential flux has been obtained from the particle count rates by dividing the energy range and, a geometric factor has been applied as suggested in Evans & Greer (2006). For that purpose, we used the 0° detectors only and did not assume on the pitch angle distribution. Please note that the MEPED electron channels are sensitive to energetic proton cross-talk (Yando et al., 2011). Consequently, we neglected the MEPED electron channels if the high-energy proton channel P7 shows more than two counts per second. The cross-talk check is done using the 2 s time resolution before averaging. The corresponding channel names are indicated by an appended "corr". As electron events are also occurring without solar energetic protons (see e.g. Nesse Tyssøy et al., 2022), the particular PC size can be determined from those electron events.

Please note that the proton detectors measure ions, but the contribution of heavier ions is expected to be negligible. Henceforth it will be assumed that the observed ion fluxes are proton fluxes.

Table 1. Channels and nominal energy range from the POES and Metop satellites which have been used. The construction of mep0e1–e2corr and mep0e2–e3corr is explained in Section 2.1.

	Instrument	Channel	Energy range
Electrons	Ted	band 4	154–224 eV
		band 8	688–1000 eV
		band 11	2.115–3.075 keV
		band 14	6.503–9.457 keV
	MEPED	mep0e1–e2corr	30–100 keV
		mep0e2–e3corr	100–300 keV
Protons	TED	band 4	154–224 eV
		band 8	688–1000 eV
		band 11	2.115–3.075 keV
		band 14	6.503–9.457 keV
	MEPED	mep0P1	30–80 keV
		mep0P2	80–240 keV
		mep0P3	240–800 keV
		mep0P4	0.8–2.5 MeV

2.2 Coordinate system and spatial grid

Particle precipitation depends on the magnetic field. Thus it is affected by geomagnetic disturbances, shows variation with local time and undergoes temporal changes. Therefore analysing statistical particle precipitation on a geographic grid is impractical. In order to eliminate (or at least minimise) these effects a magnetic coordinate system has been chosen.

For this analysis, the Modified Magnetic Apex 110 km coordinates (Richmond, 1995) have been used. These are based on the International Geomagnetic Reference Field (IGRF) model which allows for a static flux pattern in time even though the geographic position of e.g. the poles changes. The coordinates follow the magnetic field lines, meaning that a charged particle which is moving on a particular field line would always stay on the same magnetic longitude and latitude. Additionally, we chose 110 km as the reference altitude since the majority of particles get stopped here (or at least the magnetic field becomes less important than particle interactions with the atmosphere).

The benefit of these magnetic coordinates is that the particle precipitation does not show significant variation with longitude any more. Thus we can neglect the longitude and concentrate on latitudinal MLT variations.

Note that the widely used Altitude Adjusted Corrected GeoMagnetic (AACGM) coordinates and the Apex coordinates are practically identical poleward of 50° (see Fig. 7 in Laundal & Richmond, 2017) and that the herein-applied 110 km modification of the Apex coordinates has no substantial effect on the used 2° MLat × 1 h MLT grid resolution. Thus the results may be used in an AACGM grid without further transformation.

2.3 Kp binning of particle data

The Kp-index is a planetary-wide measurement of variations in the magnetic field relative to a standard quiet day value, determined at 3 h time resolution and averaged over 13 geomagnetic

stations located between 44° and 60° latitudes. Therefore it is sensitive to several current systems (e.g. the ring current) and describes magnetospheric activity with a global perspective (Bartels et al., 1939). For example, the AO boundaries are correlated with the Kp index (e.g. Carbary, 2005; Nsumei et al., 2008; Wagner & Neuhäuser, 2019).

Concerning high energetic particles, Leske et al. (2001) described the geomagnetic cutoff variations during an SPE and found a good correlation with geomagnetic indices (DST: 0.76 and, slightly better, Kp: −0.77). We choose the Kp index as it reacts better during the onset of a storm (Leske et al., 2001). Thus typical disadvantages such as the limited amount of levels and the eventual nonlinear relation with the geomagnetic cutoff variation (as suggested by Leske et al., 2001, their Fig. 6) does not impact our study since the data is binned anyway. The coarse temporal resolution may be a slight downside, but it is not expected that ionisation models run with a significantly higher temporal resolution.

A practical argument for using the Kp index is also that most particle precipitation models are based on Kp (e.g. Hardy et al., 1985; Zhang & Paxton, 2008; Wissing & Kallenrode, 2009; Sigernes et al., 2011; Wagner & Neuhäuser, 2019), thus a description of the polar flux based on Kp would allow a simple integration in such models.

The particle data in our work has been split up into 7 Kp-level groups: 0–0.7, 1–1.7, 2–2.7, 3–3.7, 4–4.7, 5–5.7, 6–9. As the Kp-levels are not equally populated (low Kp-levels occur more frequently), the amount of satellites is not constant and the local time sectors are not evenly covered, single data points (with 1 h MLT-resolution, 2° latitudinal resolution and the Kp-binning) may contain a different amount of the 16 s averages. In detail, the number of measurements at a particular bin will sum up to about 100 for the highest Kp-level and rises to more than 20,000 individual 16 s measurements for the lower levels. In minutes this means about 30 min for the highest level at every place and several days at each place for the lower levels. Due to the averaging Poisson noise is significantly reduced against single measurements and considered negligible for this study.

2.4 Recalculation of the particle flux

The starting point for this section is that the flux data is split up into a magnetic latitude vs. MLT grid and binned into different Kp levels. In addition to the fine spatial grid, we also have a combined cell for all data $|magn.lat| > 86°$ which is also binned by Kp and acts as a reference flux distribution.

As shown in Table 2 a significant fraction of the flux values consists of zeros. Especially the low energetic TED channels 11 and 14 are affected, as they consist of up to 89% zeros for quiet geomagnetic conditions. A zero in the data set simply means that the sensitive detector area is not big enough to be hit by a particle of such low flux within the 16 s integration time. In order to assess such low particle fluxes we have to increase the integration time by combining multiple 16 s measurements.

For this purpose, we replaced consecutive zeros and the first non-zero value after that with their mean. In other words, each of the contributing 16 s intervals is replaced by the mean value. Fig. 1 shows typical examples of the (sorted) recalculated flux in comparison to the (sorted) original flux. Note that the zeros that do not show up in the logarithmic scale can be identified by the missing dashed lines. As seen for 16% and 43% zeros the recalculated data set is in good agreement with the original fluxes. In addition, the low flux end shows up and the steep rise on the left indicates a low probability for very low fluxes as one would also expect from a normal distribution (or – in our case – a lognormal distribution that is mapped on a logarithmic axis). TED proton band 14 contains 88% of zeros and here the original flux is significantly modified by the recalculation. The original flux however is significantly biased by the low flux statistics. It causes zero counts in many time slots but it also causes too many counts in a few neighbouring time slots. So none of them represents the real flux. This is corrected by the recalculation.

Table 2. Fraction of zero count rates in the central polar cap flux.

Channel	0s at Kp 0–0.7	0s at Kp 6–9
TED electron band 4	10%	4%
TED electron band 8	64%	20%
TED electron band 11	87%	50%
TED electron band 14	89%	73%
mep0e1–e2corr	20%	8%
mep0e2–e3corr	8%	4%
TED proton band 4	71%	60%
TED proton band 8	43%	28%
TED proton band 11	86%	79%
TED proton band 14	88%	78%
mep0P1	16%	2%
mep0P2	5%	3%
mep0P3	28%	14%
mep0P4	71%	33%

3 Polar particle flux distribution

This section analyses the PPFD based on the recalculated flux for $|magn.lat.| > 86°$. Figure 2 shows the PPFDs for the lowest electron channel (TED electron band 4, upper panel) as well as for the highest electron channel (mep0e2–e3corr, lower panel) for different Kp levels. In both cases, the flux values spread over more than 4 orders of magnitude, showing that there is no ideal Kp-dependency on a 16-second value basis.

The TED electron band 4 (Fig. 2, top) is a typical example of a low-energy channel. Its distributions have an almost Gaussian shape (since the x-axis is logarithmic this is equivalent to a log-normal distribution in linear scale). There is an obvious Kp dependency as the total distribution shifts to higher fluxes for higher geomagnetic disturbance without a significant asymmetric component. This is also supported by the agreement of median (dashed line) and mean (solid line) of the (logarithmic) distributions.

Figure 2 (bottom) is a typical example of a high-energy particle channel. This channel does not show a shift of the total distribution but a low flux background population and an increased probability for a second high flux particle population (at about $10^{7.7}$/(MeV m^2 s sr)) that occurs at raised Kp only (slightly enhanced for Kp 5–5.7, significantly enhanced for Kp 6–9).

While the shape of the low Kp background population at low flux stays almost the same throughout the different Kp levels, the fraction of the high flux population determines the

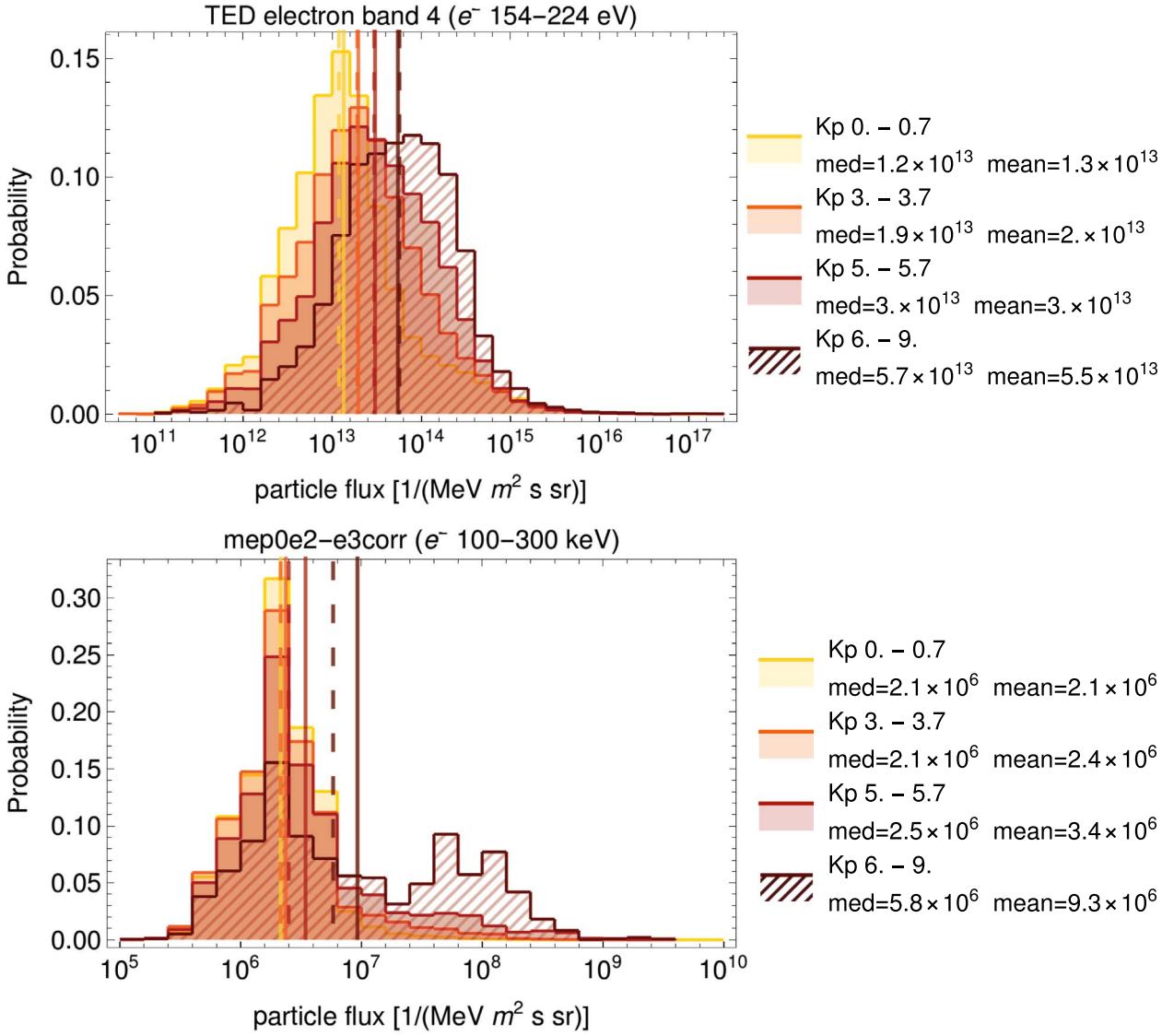

Figure 2. The figure shows typical flux distributions in the central polar cap (≥86° north and south) for selected Kp levels. The lowest electron channel is presented in upper panel, the highest electron channel is given in the lower panel. The dashed lines are the corresponding medians and the solid lines are the means.

contribution of these two populations in every Kp level. For higher Kp levels the intense flux fractions rise, shifting the mean to higher fluxes, while the median in many cases is not an ideal indicator for the combined distributions.

This second population can be attributed to solar particle events (SPEs). The SEP fraction should show a higher fluctuation than the background population. Higher Kp-level groups are more affected by SEPs as both have the same driver. These can be gradual events that have their origin in coronal mass ejection-driven shocks and may last for a couple of days or short-term impulsive events caused by flares (Cane et al., 1986). It should be noted that a gradual event may also be accompanied by energetic storm particles (ESPs) that are accelerated at a greater distance to the Sun and that appear directly at the passage of the geomagnetic storm (Cohen, 2006). According to Kallenrode 2003, there should be a continuous transition between gradual and impulsive events. Therefore, SEPs and geomagnetic disturbances often come in pairs. Figure 2 shows this in form of the second maximum (of SEPs) for Kp 6–9 which is clearly separated from the non-SPE population.

The channels in Figure 2 have been selected because the amount of zero counts is rather low in order to present unbiased data. Using recalculated fluxes the aforementioned statements on the different behaviour of low and high energetic channels also hold for the channels that contain a significant fraction of zero counts (compare Table 2 and following discussion of Fig. 3).

Figure 3 extends the presentation of the flux probabilities in Figure 2 to all particles and Kp combinations in this study. Some of the particle flux distributions show multiple narrow peaks within a particular flux range, especially the MEPED proton channels between $2 \times 10^4 - 10^7$/(MeV m^2 s sr). This is an artefact caused by the limited flux resolution and can also be identified in Figure 1 (as stepped function of mep0P1).

The typical evolution of the low energetic particle flux distribution with Kp (as also shown in Fig. 2, top) can be identified

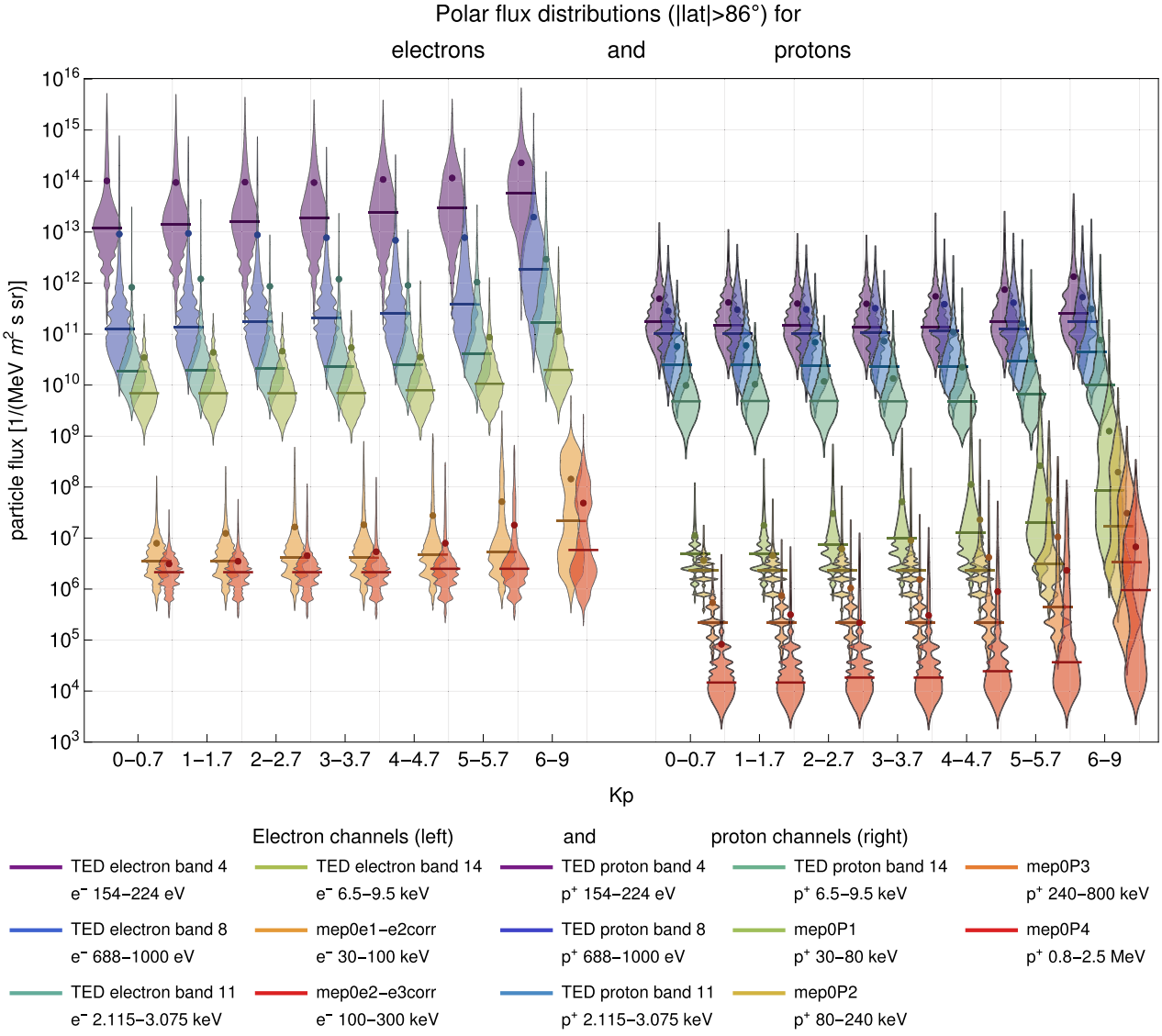

Figure 3. The figure shows the central polar cap flux distributions (≥86° north and south). The median is indicated by a horizontal line, the dots represent the mean of the respective distribution.

for all TED channels. This is also indicated by the median (horizontal line in Fig. 3) which steadily increases with Kp (most obvious for TED electrons).

In contrast to that the second particle population is seen in all MEPED channels for the highest Kp-level and to some degree also in the second highest. The relative contribution of the second particle population increases with energy, which is clearly seen for protons. For the highest proton channel in this study, mep0P4, the SPE contribution at Kp 6–9 is even bigger than the non-SPE population. Concerning the relative contribution of the SPE population there might be a smooth transition from the clearly visible fraction in the high energetic MEPED proton channels to an insignificant component in the low energetic TED channels. Especially for the high energetic channels (protons and electrons) the median is relatively stable for low Kp but jumps up at the highest geomagnetic disturbance.

Note that a good argument for the recalculated flux is given by the distributions of TED electron bands 4 and 14. Even though TED 14 contains 89% zeros (for the lowest Kp-level), its distribution is similar to that of TED 4 which just contains 10% of zeros.

Note also that the dot marks the non-logarithmic mean of the distribution. Given the higher impact of high flux values the non-logarithmic mean is more sensible for the second particle population and thus shows a stronger and more even Kp dependence for the MEPED channels than the median.

4 Spatial extent of the polar particle flux distribution

We assume that a similar probability for the same flux in neighbouring bins (throughout the whole particle flux spectrum) makes it very likely to detect a similar flux (within typical statistical variation) at any given time step. Or, from another perspective, it sounds very unlikely to end up with the same

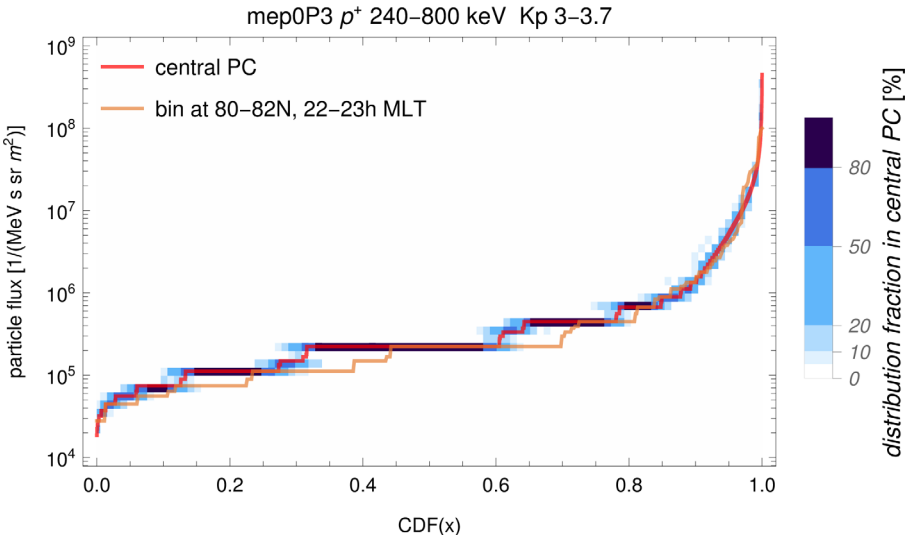

Figure 4. The figure shows the comparison of the central polar cap flux distribution (≥86° north and south) and a single bin. The difference is indicated by the Δ-test. The blue-shaded area counts the fraction of single bin cumulative distribution functions (CDFs) inside the central polar cap as indication of the low statistical variation.

cumulated flux probability in the spatial bins if these bins show a systematic flux difference in simultaneous measurements as expected e.g. for different particle sources.

Following that assumption, the spatial extent of the PPFD area is of interest for particle precipitation modelling as a few particle measurements inside this area might be used to describe the particle flux in the whole PPFD area for a particular time. Given that the region is significantly bigger than $|magn.lat.| > 86°$ it might also be used to further increase particle statistics. The next section presents the method that is used to determine the PPFD area, while Section 4.2 presents the results.

4.1 Method

The spatial extent of the PPFD area is determined by comparing the flux distributions in all bins to the reference flux distribution in $|magn.lat.| > 86°$. The total time of measurement of the reference distribution is significantly higher than for a single bin, ranging from 20 h for the highest Kp-level to 94 days for the lowest level.

The particle distributions may contain multiple peaks (as for MEPED channels at high Kp) or stepped functions in case of the limited flux resolution which ends up in non-normal distributions. Thus we needed a comparison test that expresses the similarity of two arbitrary distributions. Our test works as follows: First, the measurements of the reference distribution as well as the test-distribution are sorted. As the particle flux varies on orders of magnitude, we use the logarithmic values. The sorted order of the flux observations is scaled to the range 0–1 (see *x*-axis in Fig. 4). This essentially is a cumulative distribution function (CDF). In the second step, the absolute (logarithmic) flux difference between every point of the reference population and the interpolated reference distribution at the same point is determined. The sum of all points results in a characteristic value for the similarity of the two distributions, labelled as Δ:

$$\Delta = \frac{\Sigma_i |f_{\text{test},\,i} - f_{\text{ref, interpolated at } i}|}{N_{\text{test}}}, \tag{1}$$

with f being the logarithmic particle fluxes and N_{test} being the number of measurements in the test data set. In principle the Δ-test integrates the area between the two distribution curves, but at the points of the test distribution. We accepted Δ-tests with 10 or more data points per bin.

The Δ-test has been applied to every bin, ending up with a spatial matrix expressing the similarity. As already mentioned in Section 2.3 the bins are not equally populated. Given the uneven spatial coverage of satellites, neighbouring bins may be populated by zero, dozens or even ten thousand data points. In order to fill the matrix and reduce the impact of sparsely populated bins on the accuracy of the Δ-test we applied the following method: Bins with less than 10 data points (no Δ-test) are identified as well as those that consist of less than 1/10th of the amount of data points compared to neighbouring MLT bins on the same latitude. These statistically poor bins are recalculated by a weighted linear fit, where the weighting is based on the number of measurements in the used bins. For every recalculated bin the closest three neighbours on both sides as well as the same bin (if a Δ-test has been made) enter the regression. As a result, the similarity matrix is filled and outliers that may occur due to sparely populated bins are recalculated while preserving MLT variations and keeping bins with good statistics untouched.

The similarity matrix now contains Δ-test values for every bin and we need to set a threshold that defines the bins which show the same flux distribution as the PPFD. The threshold also needs to be Kp-dependent as the statistical flux fluctuations increase with Kp and in addition to that the lower number of data points in high Kp levels also reduces the accuracy of the Δ-test. The standard deviation σ of the Δ-test values for all bins inside $|magn.lat.| > 86°$ should provide a good estimate of the statistical variation that appears inside the PPFD area.

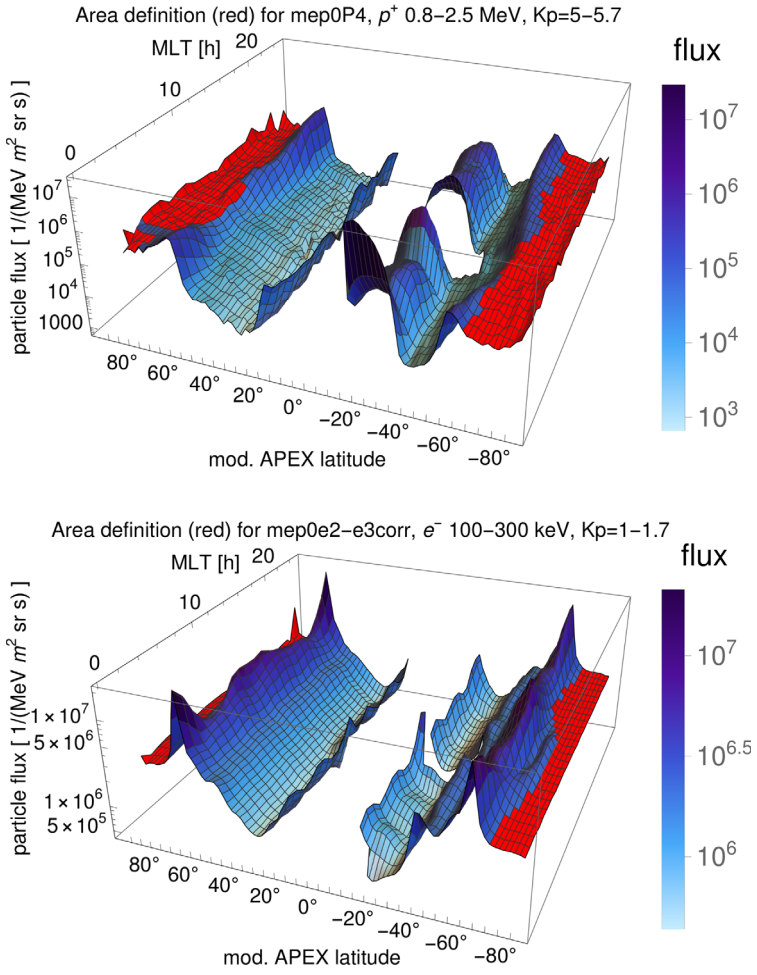

Figure 5. Bin-averaged particle flux distribution for the entire data set for a particle channel with weak auroral contribution (top) and strong auroral contribution (bottom). The PPFD area is indicated in red.

Consequently, we selected all bins with $\Delta < 3\sigma$ for a preliminary PPFD area.

The statistical variation of the single CDFs inside the $|magn.lat.| > 86°$ is shown as a shaded area in Figure 4. The colour indicates the fraction of CDFs inside a corresponding flux range. The variation inside the central polar cap CDFs is extremely small. In most cases, a single flux range contains more than 80% of the CDFs. Thus 18 years seem to be more than enough to get a good statistical representative flux distribution even on a single spatial bin basis.

Continuing with the preliminary PPFD area, we apply a simple algorithm in order to prevent single excluded bins inside the PPFD area as well as to prevent outliers. Starting from the maximum of the auroral precipitation, two patterns are identified for each MLT sector on the path towards the magnetic pole: if a bin is specified as a preliminary PPFD area followed by three bins that are not specified as such, this is ignored as probably being an outlier. If a bin is not specified as a preliminary PPFD area followed by a bin that belongs to a preliminary PPFD area, the latter one is accepted as a lower latitude boundary of the (final) PPFD area in this MLT sector. This results in the PPFD areas presented in the following part of the paper.

4.2 Results

Figure 5 shows the PPFD area (marked in red) mapped on the bin-averaged flux distribution. In particular, for Figure 5 (bottom) the Δ-test selects a region that is not only similar in the shape of the flux distribution but the PPFD area is also very similar in terms of the logarithmic mean. Regarding that Figure 5 (top) is based on significantly fewer data points (which also contain higher fluctuations due to elevated Kp) this statement also holds for mep0P4 at high Kp levels.

Figure 5 (bottom) is a typical example of a particle channel with a significant auroral particle contribution. Here the PPFD area is enclosed by high average flux. Figure 5 (top) in contrast shows a highly energetic proton channel, which has a relatively small auroral component. Here the flux in the bins surrounding the PPFD area is just slightly enhanced except for the morning sector, where no elevated flux average can be found. As seen in Figure 3 the SPE contribution for mep0P4 is rather high, which leads to a high mean flux plateau in the PPFD area.

Focusing on the PPFD area, the polar plots in Figure 6 show the proton channel mep0P3 for both hemispheres. This channel stands paradigmatic for the hemispheric differences in all

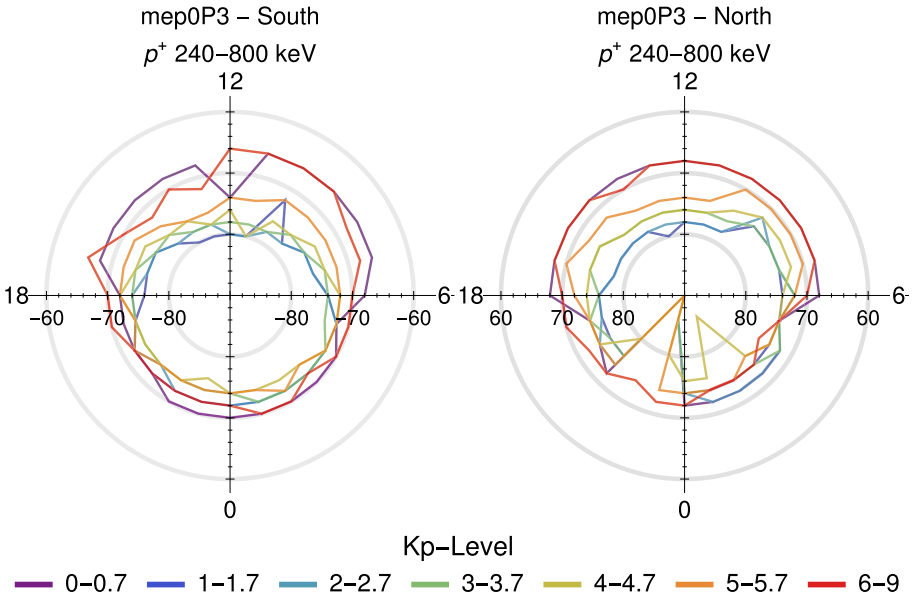

Figure 6. The boundary of empirically determined PPFD area for the proton channel mep0P3 is shown for southern (left) and northern (right) hemispheres at different Kp levels in MLAT vs. MLT coordinates. The polar plots are centred on one of the magnetic poles.

particle channels. Typically both hemispheres show rather similar PPFD areas. Noticeable differences are restricted to the MLT range 20–23 h, in particular to 22–23 h where the border in the northern hemisphere approaches the geomagnetic pole. In rare cases, the MLT range of 2–4 h may also be affected. Given that many particle channels and Kp combinations show this behaviour, we refer to Figure 4 which shows the flux distribution of a bin inside this anomaly (at 80–82N, 22–23 h MLT) in comparison to the reference PPFD. Even though the local time sector close to midnight in the north is not well covered by satellite data, we can exclude this technical reason. There are sufficient data points to expect an adequate Δ-test. In contrast, Figure 4 clearly shows that especially the centre of the bin's particle distribution is shifted to a lower flux in comparison to the PPFD.

For the electron channels – which show a similar pattern – the reason might be the polar rain gap that is known to occur in the same region. It was mentioned first by Torbert et al. (1981). Section 2 in Newell et al. (2009) describes a midnight-noon gradient in polar rain. A possible source is discussed in Newell and Meng (1990) as being reconnected field lines in the magnetotail lobes. Hemispheric asymmetries in the polar rain are reported as well (Yeager & Frank, 1976). The reason for the similar proton discrepancy however is not known.

We may conclude that the PPFD area can represent the particle flux in the whole area, but especially in the northern hemisphere bins with different flux distributions are excluded, which effectively declines the PPFD area in the midnight-noon direction. Apart from that there are no characteristic differences between the hemispheres. Thus the latter part of the paper discusses results for the southern hemisphere only.

Figure 7 gives an overview of the PPFD area for different energy channels and its Kp dependence. While the upper panel shows protons with increasing particle energy from left to right, the lower panel presents the same for electrons. Note that the empirical PPFD areas are given in Tables S1–S3 in the Supplementary materials.

We start with the *similarities found in the PPFD areas of all channels*. The centre of the PPFD area is clearly shifted towards midnight for low Kp levels (about 85°–87°S). This offset is a well-known feature that also can be observed for the electron polar cap since auroral oval studies by Feldstein & Starkov (1967) or as shown in a statistical analysis by Bikkuzina et al. (1998).

We continue with the description of the Kp dependence of the *PPFD area for low energetic protons and electrons* as measured with the TED channels as well as mep0e1–e2corr, mep0P1 and mep0P2 (latter three not shown). For increasing Kp levels the centre is moving towards the afternoon sector (low energy electrons, see Fig. 7: TED electron band 8/14) or evening sector (low energy protons, see Fig. 7: TED proton band 11). During the shift the PPFD area is increasing in size, roughly doubling it. There is a tendency of the PPFD area to enlarge towards the direction where the auroral precipitation is weakest. For TED electron band 14, this is 12–15 MLT (compare Fig. 3 in Yakovchuk & Wissing, 2019), and for the lowest three TED proton bands, this is the evening sector (compare upper panels of Fig. 4 in Yakovchuk & Wissing, 2019). Apart from that all low energetic channels – regardless of particle species – have a very similar PPFD area for a given Kp level. The upper energy threshold for this behaviour is about 240 keV for protons and 100 keV for electrons. Note that the energy threshold is taken from the channels' energy range (see Table 1).

Above these energy thresholds, we can see an increase in the size of the PPFD area that sometimes depends on particle energy. For protons, this statement is justified by two particle channels, and for the electrons just one channel above the threshold is available. We can identify the enlargement of the PPFD area with Kp. However, this does not hold for all Kp levels. The PPFD area of the lowest Kp-level (for mep0P4 the two lowest Kp levels) are the clear exception and forms a

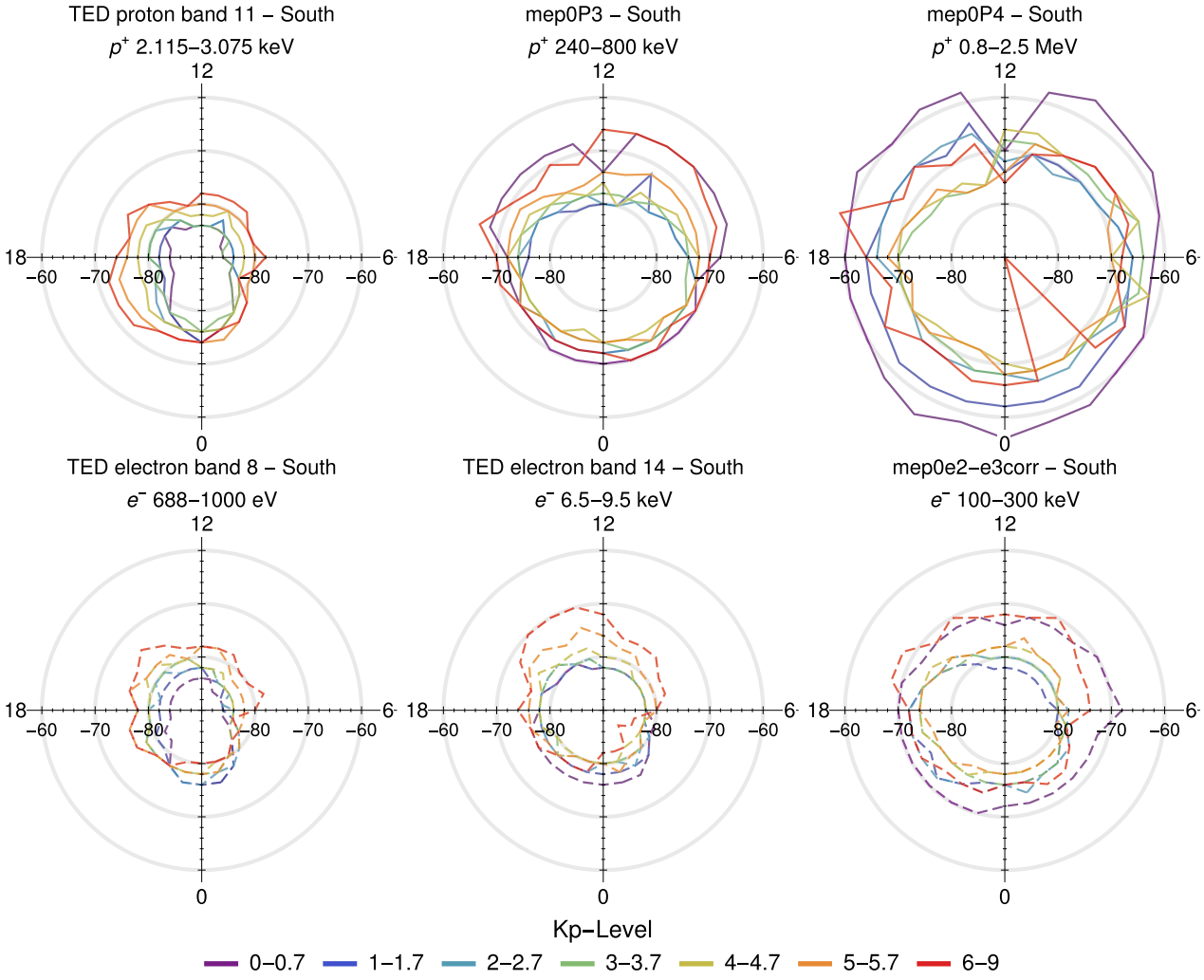

Figure 7. Position of PPFD areas for selected proton channels (top row) selected electron channels (bottom row). Data for all Kp levels are shown in MLAT-MLT coordinates, where MLAT is a modified Apex magnetic latitude and MLT is the corresponding local time.

large PPFD area, partly even bigger than the one of Kp 6–9. The reason is the missing auroral particle precipitation at low Kp in these channels. As soon as the Kp-level rises the auroral component changes the particle distribution and thus the Δ-test value increases. For low-energy channels the auroral component is always significant, thus these channels are not affected.

Note that the PPFD area is a lower estimate of the region where similar flux can be found for a given time. Polar rain, SEP and auroral flux determine the size of the PPFD area. However, these populations do not have the same boundary. Thus the PPFD area is defined as a region where the SEP population and polar rain may occur but no significant auroral precipitation is detected.

In addition to that temporal variations may occur. Substorms for example have a different precipitation pattern (Figs. 3–5 in Yakovchuk & Wissing, 2019) and thus may decrease the size of the PPFD area in a multi-year flux distribution. Fortunately, these effects do not limit our results. The paper aims to define an area that has the same flux characteristics. In accordance with this requirement, it is an advantage to exclude regions that (sometimes) show different particle populations than the reference distribution does.

5 Inter-comparison of our results

The spatial extent of the PPFD area is restricted by the occurrence of particle populations. The existence of an auroral particle distribution should be a major component that delimits the PPFD area. Therefore we decided to compare our results with Kp-dependent auroral UV measurements from Figures 4 and 6 in Carbary (2005) that are taken as an indicator for auroral precipitation.

Using near-global images of the Polar Ultraviolet Imager (Torr et al., 1995) in the Northern hemisphere Carbary (2005) obtained the auroral boundaries. He used more than 40,000 UV images grouped by Kp-level during 4 months of 1997. He gridded the data in corrected geomagnetic latitude (CGM-MLAT) and MLT, a coordinate system being very similar to modified Apex magnetic coordinates (Baker & Wing, 1989), therefore we can directly compare the results. Among other things, Carbary (2005) identified the polar border of the mean UV aurora.

Figure 8 shows the corresponding comparison. The top panel presents all proton PPFD areas for selected Kp levels.

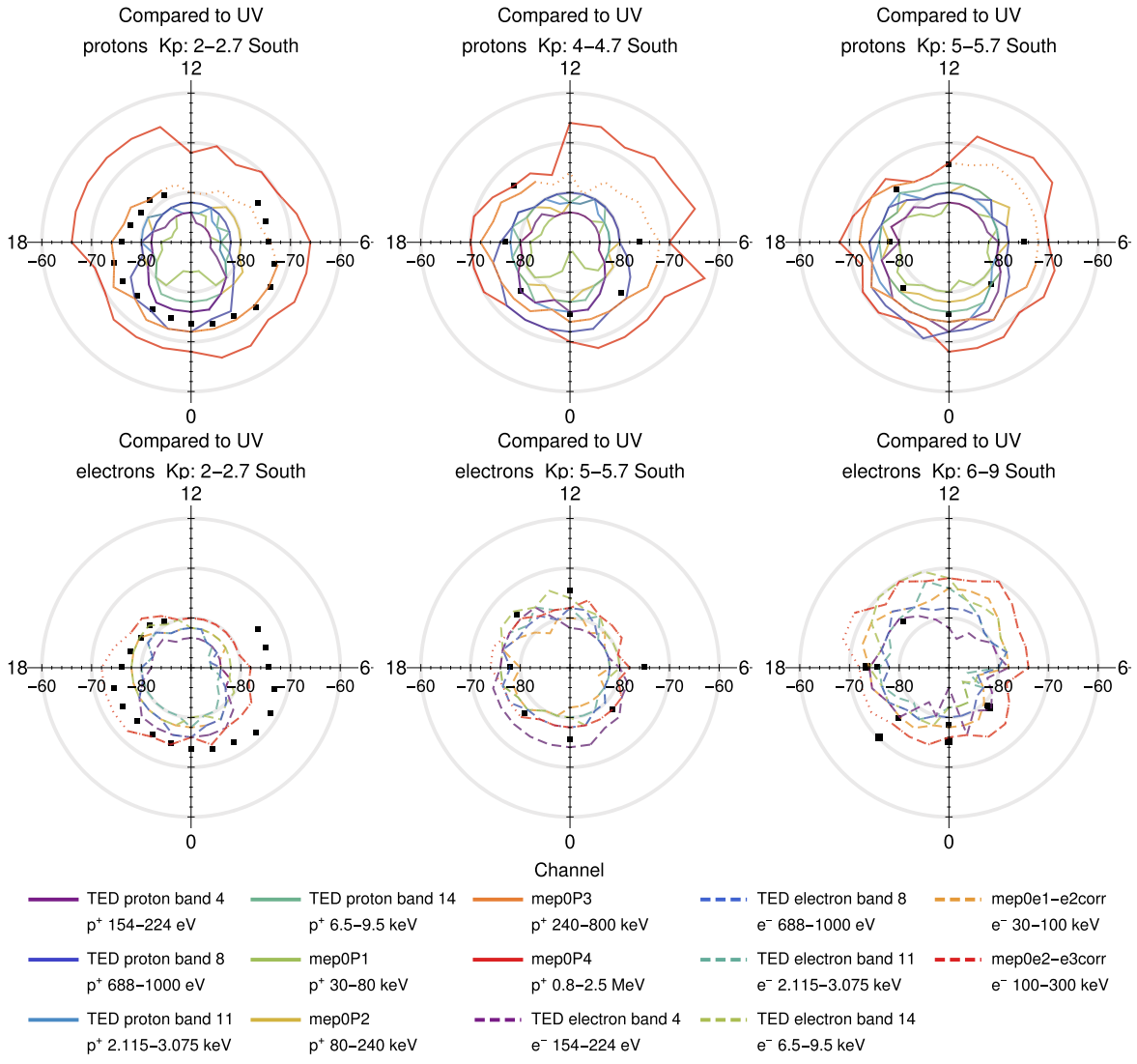

Figure 8. Comparison of the PPFD areas from all channels at selected Kp levels with the corresponding poleward boundary of the auroral UV measurements (black squares) from Figures 4 and 6 in Carbary (2005).

Additionally, the poleward position of the UV aurora is indicated by black squares. Note that we apply the results of Carbary (2005) to the southern hemisphere. However, the northern hemisphere has the same particle characteristics (see Fig. 6). The lower panel shows electrons with the same setup.

Starting with the electrons (lower panel of Fig. 8), practically all PPFD areas are located poleward of the AO boundary. This especially holds for Kp values up to 5.7 (left and middle column of Fig. 8). The explanation is straightforward as the additional auroral particle distribution increases the Δ-test value. In more detail (see left column, lower panel of Fig. 8), the PPFD area is shifted towards the evening sector in relation to the UV boundary. The reason is the weak auroral precipitation in specific MLTs and has already been noted in the discussion of Figure 7. For illustration we marked MLTs of very weak auroral electron/proton precipitation by a dotted line using the electron channel mep0e2–e3corr (red) and the proton channel mep0P3 (orange). The information on the intensity of the auroral precipitation has been taken from Figures 3 and 4 in Yakovchuk & Wissing (2019). Precisely in these MLTs of very weak auroral contribution, the PPFD area surpassed the UV boundary. In contrast, the enhanced auroral precipitation on the morning side may lead to a bigger distance of the PPFD area. This can be explained by the chance that high flux from the auroral oval may contribute to neighbouring bins when the AO is shifting during geomagnetic fluctuations (substorms for example). On the evening side, however, the weak AO cannot affect neighbouring bins in a similar way.

For Kp 6–9 (lower panel, right column) the AO boundary does not limit the spatial extent of the PPFD area in all channels. Especially for mep0e2–e3corr the enhanced fraction of the SPE population in comparison to the relatively weak auroral distribution leads to a PPFD area that stretches over the UV boundary towards the day side. In the morning sector, the PPFD area is significantly enlarged as well but a value of the UV boundary comparison is missing. Note that there are two sets of squares in this figure, a smaller one indicating the UV boundary for Kp 6–6.7 and a bigger square for Kp 7–8.

The protons in Figure 8 (upper panel) can also be divided into a group of low energetic channels (up to 240 keV) where the occurrence of an auroral population limits the spatial extent of the PPFD area. The mep0P3 channel shows a bigger PPFD area that mostly matches the poleward AO boundary. Only for enhanced Kp levels starting from Kp 4–4.7 the UV boundary is crossed. For the highest proton channel as well as for an increasing amount of channels with rising Kp the auroral precipitation becomes negligible for the whole flux distribution and thus the UV boundary does not limit the spatial extent of the PPFD area any more.

6 Conclusions

This work describes the particle flux distribution at the geomagnetic poles and shows a method to find areas with similar flux distributions based on measurements from NOAA POES/Metop spacecraft during 2001–2018. The following findings have been made:

1. Even high fractions of zero count rates can be recalculated using longer integration times.
2. The PPFD for low energy channels shows a gradual flux increase with rising geomagnetic disturbance. In high-energy channels, the background population is mostly unaltered while a separate SPE population adds up with increasing Kp.
3. The Δ-test determines the similarity of arbitrary distributions.
4. Hemispheric differences of the PPFD area are mostly negligible in the chosen coordinate system (modified Apex 110 km). A characteristic exception throughout different channels and Kp levels can be found in the northern pre-midnight sector. The centre of the flux distribution is shifted to lower flux levels. For electrons, this might be attributed to polar rain asymmetries.
5. The PPFD area seems to be constant below a characteristic energy threshold. For electrons, the threshold is about 100 keV and for protons about 240 keV. Above that energy the PPFD area increases.
6. The PPFD area shows a clear enlargement with geomagnetic disturbance. But at Kp 0–0.7 channels without significant auroral precipitation may exhibit an exceptionally large PPFD area.
7. The centre of the PPFD area is shifted towards midnight. With increasing Kp it shifts towards the geomagnetic pole (protons) or the afternoon sector (electrons). The asymmetry can be explained by the intensity of the surrounding auroral precipitation.
8. As far as low energetic particles are considered the PPFD area is mainly restricted by the auroral particle flux.
9. The coordinates of the PPFD area are appended as Supplementary materials. Since the PPFD is found in all these bins, we also expect similar fluxes for a given time. Thus measurements at any place inside the PPFD area should be a good proxy for the whole PPFD area.

Please note that the PPFD area is not the same as the SEP plateau region. Given that the PPFD contains all particle populations at the geomagnetic pole, the PPFD area can be defined as the intersection of the polar rain area and the SEP plateau region, while bins with significant auroral populations are removed. Therefore, the PPFD area is expected to be smaller than the SEP plateau region.

Acknowledgements. This work is funded by the German Science Foundation (DFG project WI4417/2-1). J.M. Wissing also thanks to support from the German Aerospace Center (DLR). We acknowledge financial support by Deutsche Forschungsgemeinschaft and Universität Rostock within the funding programme Open Access Publishing. The authors acknowledge the NOAA National Centers for Environmental Information (https://ngdc.noaa.gov/stp/satellite/poes/dataaccess.html) for the POES and Metop particle data used in this study. The editor thanks three anonymous reviewers for their assistance in evaluating this paper.

Supplementary materials

The supplementary information of this article is available at https://www.swsc-journal.org/10.1051/swsc/2023009/olm.

The empirical definition of the PPFD area represents a region with similar flux characteristics. In consequence measurements at any point inside this area may be used to represent the whole PPFD area. This may be of special interest to particle precipitation/ionisation models. Tables S1, S2 and S3 in the supplementary information contain area definitions in MLT and Modified Magnetic Apex 110 km coordinates (based on IGRF and similar to AACGM coordinates) and can thus be converted into geographic coordinates for arbitrary times.

Table S1: Magnetic apex latitude and MLT of the polar particle flux distribution area equatorial boundary for low energy electrons in relation to Kp.

Table S2: Magnetic apex latitude and MLT of the polar particle flux distribution area equatorial boundary for high energy electrons and low energy protons.

Table S3: Magnetic apex latitude and MLT of the polar particle flux distribution area equatorial boundary for high energy protons.

References

Aikio AT, Pitkänen T, Kozlovsky A, Amm O. 2006. Method to locate the polar cap boundary in the nightside ionosphere and application to a substorm event. *Ann Geophys* **24(7)**: 1905–1917. https://doi.org/10.5194/angeo-24-1905-2006.

Baker JB, Clauer CR, Ridley AJ, Papitashvili VO, Brittnacher MJ, Newell PT. 2000. The nightside poleward boundary of the auroral oval as seen by DMSP and the ultraviolet imager. *J Geophys Res* **105(A9)**: 21267–21280. https://doi.org/10.1029/1999JA000363.

Baker KB, Wing S. 1989. A new magnetic coordinate system for conjugate studies at high latitudes. *J Geophys Res* **94(A7)**: 9139–9143. https://doi.org/10.1029/JA094iA07p09139.

Bartels J, Heck NH, Johnston HF. 1939. The three-hour-range index measuring geomagnetic activity. *Terr Magn Atmos Electr* **44(4)**: 411–454. https://doi.org/10.1029/TE044i004p00411.

Bikkuzina GR, Sergeev VA, Bösinger T. 1998. Particle boundaries during a solar electron event. In: *Polar cap boundary phenomena*, Moen J, Egeland A, Lockwood M, (Eds.), Springer, Dordrecht,

The Netherlands, pp. 355–367. ISBN 978-94-011-5214-3. https://doi.org/10.1007/978-94-011-5214-3_27.

Blanchard GT, Lyons LR, Samson JC, Rich FJ. 1995. Locating the polar cap boundary from observations of 6300 Å auroral emission. *J Geophys Res* **100(A5)**: 7855–7862. https://doi.org/10.1029/94JA02631.

Bornebusch J, Wissing J, Kallenrode M-B. 2010. Solar particle precipitation into the polar atmosphere and their dependence on hemisphere and local time. *Adv Space Res* **45(5)**: 632–637. https://doi.org/10.1016/j.asr.2009.11.008.

Cane HV, McGuire RE, von Rosenvinge TT. 1986. Two classes of solar energetic particle events associated with impulsive and long-duration soft X-ray flares. *Astrophys J* **301**: 448. https://doi.org/10.1086/163913.

Carbary JF. 2005. A Kp-based model of auroral boundaries. *Space Weather* **3(10)**: S10001. https://doi.org/10.1029/2005SW000162.

Chisham G, Freeman MP, Sotirelis T. 2004. A statistical comparison of SuperDARN spectral width boundaries and DMSP particle precipitation boundaries in the nightside ionosphere. *Geophys Res Lett* **31(2)**: L02804. https://doi.org/10.1029/2003GL019074.

Cohen CMS. 2006. Observations of energetic storm particles: an overview. In: *Solar eruptions and energetic particles*, Gopalswamy N, Mewaldt R, Torsti J, (Eds.), American Geophysical Union (AGU), pp. 275–282. ISBN 9781118666203. https://doi.org/10.1029/165GM26.

Craven JD, Frank LA. 1987. Latitudinal motions of the aurora during substorms. *J Geophys Res* **92(A5)**: 4565–4574. https://doi.org/10.1029/JA092iA05p04565.

Dungey JW. 1961. Interplanetary magnetic field and the auroral zones. *Phys Rev Lett* **6(2)**: 47–48. https://doi.org/10.1103/PhysRevLett.6.47.

Evans D. 2008. General update – SEM-2 performance on the operating satellites during 2007. *Technical report*. National Oceanic and Atmospheric Administration. https://satdat.ngdc.noaa.gov/sem/poes/docs/status_2008-01-10.pdf.

Evans DS, Greer MS. 2006. *Polar orbiting environmental satellite space environment monitor – 2, instrument descriptions and archive data documentation*. National Oceanic and Atmospheric Administration, NOAA Space Environ. Lab, Boulder, Colorado, USA. Version 2.0. https://satdat.ngdc.noaa.gov/sem/poes/docs/sem2_docs/2006/SEM2v2.0.pdf.

Evans L, Stone E. 1972. Electron polar cap and the boundary of open geomagnetic field lines. *J Geophys Res* **77(28)**: 5580. https://doi.org/10.1029/JA077i028p05580.

Feldstein YI, Starkov GV. 1967. Dynamics of auroral belt and polar geomagnetic disturbances. *Planet Space Sci* **15(2)**: 209–229. https://doi.org/10.1016/0032-0633(67)90190-0.

Gary JB, Zanetti LJ, Anderson BJ, Potemra TA, Clemmons JH, Winningham JD, Sharber JR. 1998. Identification of auroral oval boundaries from in situ magnetic field measurements. *J Geophys Res* **103(A3)**: 4187–4198. https://doi.org/10.1029/97JA02395.

Gussenhoven MS, Brautigam DH. 1994. Boundary populations in the polar caps. *J Atmos Terr Phys* **56(2)**: 167–183. https://doi.org/10.1016/0021-9169(94)90028-0.

Hardy DA, Gussenhoven MS, Holeman E. 1985. A statistical model of auroral electron precipitation. *J. Geophys. Res.* **90**: 4229–4248. https://doi.org/10.1029/JA090iA05p04229.

Herbst K, Kopp A, Heber B. 2013. Influence of the terrestrial magnetic field geometry on the cutoff rigidity of cosmic ray particles. *Ann Geophys* **31(10)**: 1637–1643. https://doi.org/10.5194/angeo-31-1637-2013.

Johnsen MG, Lorentzen DA, Holmes JM, Løvhaug UP. 2012. A model based method for obtaining the open/closed field line boundary from the cusp auroral 6300 Å[OI] red line. *J Geophys Res Space Phys* **117(A3)**: A03319. https://doi.org/10.1029/2011JA016980.

Kallenrode M-B. 2003. Current views on impulsive and gradual solar energetic particle events. *J Phys G Nucl Part Phys* **29(5)**: 965–981. https://doi.org/10.1088/0954-3899/29/5/316.

Kauristie K, Weygand J, Pulkkinen TI, Murphree JS, Newell PT. 1999. Size of the auroral oval: UV ovals and precipitation boundaries compared. *J Geophys Res* **104(A2)**: 2321–2332. https://doi.org/10.1029/1998JA900046.

Laundal KM, Richmond AD. 2017. Magnetic coordinate systems. *Space Sci Rev* **206(1–4)**: 27–59. https://doi.org/10.1007/s11214-016-0275-y.

Leske RA, Mewaldt RA, Stone EC, von Rosenvinge TT. 2001. Observations of geomagnetic cutoff variations during solar energetic particle events and implications for the radiation environment at the space station. *J Geophys Res Space Phys* **106(A12)**: 30011–30022. https://doi.org/10.1029/2000JA000212.

Lukianova R, Kozlovsky A. 2011. IMF B_y effects in the plasma flow at the polar cap boundary. *Ann Geophys* **29(7)**: 1305–1315. https://doi.org/10.5194/angeo-29-1305-2011.

Lukianova R, Kozlovsky A. 2013. Dynamics of polar boundary of the auroral oval derived from the IMAGE satellite data. *Cosm Res* **51(1)**: 46–53. https://doi.org/10.1134/S0010952513010061.

McEwen DJ. 1998. Polar cap phenomena and their relation to boundary layers and the IMF. In: *Polar cap boundary phenomena*, Moen J, Egeland A, Lockwood M, (Eds.), Springer, Dordrecht, The Netherlands, pp. 271–280. https://doi.org/10.1007/978-94-011-5214-3_20.

Meng C-I, Makita K. 1986. Dynamic variations of the polar CAP. In: *Solar wind magnetosphere coupling, vol. 126 of Astrophysics and Space Science Library*, Kamide Y, Slavin JA, (Eds.), Terra Scientific Publishing Company/D. Reidel Publishing Company, Tokyo, Japan/Dordrecht, The Netherlands, pp. 605–631. ISBN 90-277-2303-6.

Milan SE, Lester M, Cowley SWH, Oksavik K, Brittnacher M, Greenwald RA, Sofko G, Villain JP. 2003. Variations in the polar cap area during two substorm cycles. *Ann Geophys* **21(5)**: 1121–1140. https://doi.org/10.5194/angeo-21-1121-2003.

Murphree JS, Elphinstone RD, Cogger LL, Hearn D. 1991. Viking optical substorm signatures. In: *Magnetospheric substorms, vol. 64 of Geophysical Monograph Series*, Kan JR, Potemra TA, Kokubun S, Iijima T, (Eds.), American Geophysical Union, Washington, DC, pp. 241–255. https://doi.org/10.1029/GM064p0241.

Nesse Tyssøy H, Sinnhuber M, Asikainen T, Bender S, Clilverd MA, et al. 2022. HEPPA III intercomparison experiment on electron precipitation impacts: 1. Estimated ionization rates during a geomagnetic active period in April 2010. *J Geophys Res Space Phys* **127(1)**: e2021JA029128. https://doi.org/10.1029/2021JA029128.

Newell PT, Liou K, Wilson GR. 2009. Polar cap particle precipitation and aurora: review and commentary. *J Atmos Sol Terr Phys* **71(2)**: 199–215. https://doi.org/10.1016/j.jastp.2008.11.004.

Newell PT, Meng C-I. 1990. Intense keV energy polar rain. *J Geophys Res Space Phys* **95(A6)**: 7869–7879. https://doi.org/10.1029/JA095iA06p07869.

Nsumei PA, Reinisch BW, Song P, Tu J, Huang X. 2008. Polar cap electron density distribution from IMAGE radio plasma imager measurements: empirical model with the effects of solar illumination and geomagnetic activity. *J Geophys Res Space Phys* **113(A1)**: A01217. https://doi.org/10.1029/2007JA012566.

Richmond AD. 1995. Ionospheric electrodynamics using magnetic apex coordinates. *J Geomag Geoelectr* **47**: 191–212. https://doi.org/10.5636/jgg.47.191.

Scholer M. 1972. Polar-cap structures of solar protons observed during the passage of interplanetary discontinuities. *J Geophys Res (1896–1977)* **77(16)**: 2762–2769. https://doi.org/10.1029/JA077i016p02762.

Sergeev VA. 1990. Polar cap and cusp boundaries at day and night. *J Geomag Geoelectr* **42(6)**: 683–695. https://doi.org/10.5636/jgg.42.683.

Sergeev VA, Kuznetsov SN, Gotseliuk IV. 1987. Dynamics of the high-latitude magnetospheric structure as given by solar electron data. *Geomagn Aeron* **27**: 440–447.

Shirai H, Maezawa K, Fujimoto M, Mukai T, Yamamoto T, Saito Y, Kokubun S. 1998. Entry process of low-energy electrons into the magnetosphere along open field lines: polar rain electrons as field line tracers. *J Geophys Res Space Phys* **103(A3)**: 4379–4390. https://doi.org/10.1029/97JA02031.

Sigernes F, Dyrland M, Brekke P, Chernouss S, Lorentzen DA, Oksavik K, Deehr CS. 2011. Two methods to forecast auroral displays. *J Space Weather Space Clim* **1(1)**: A03. https://doi.org/10.1051/swsc/2011003.

Smart DF, Shea MA, Gall R. 1969. The daily variation of trajectory-derived high-latitude cutoff rigidities in a model magnetosphere. *J Geophys Res (1896–1977)* **74(19)**: 4731–4738. https://doi.org/10.1029/JA074i019p04731.

Sotirelis T, Ruohoniemi JM, Barnes RJ, Newell PT, Greenwald RA, Skura JP, Meng CI. 2005. Comparison of SuperDARN radar boundaries with DMSP particle precipitation boundaries. *J Geophys Res Space Phys* **110 (A6)**: A06302. https://doi.org/10.1029/2004JA010732.

Torbert RB, Cattell CA, Mozer FS, Meng C-I. 1981. The boundary of the polar cap and its relation to electric fields, field-aligned currents, and auroral particle precipitation. In: *Physics of auroral arc formation, vol. 25 of Geophysical Monograph Series*, Akasofu S-I, Kan JR, (Eds.), American Geophysical Union (AGU), pp. 143–153. ISBN 9781118664360. https://doi.org/10.1029/GM025p0143.

Torr MR, Torr DG, Zukic M, Johnson RB, Ajello J, et al. 1995. A far ultraviolet imager for the international solar-terrestrial physics mission. *Space Science Rev* **71(1–4)**: 329–383. https://doi.org/10.1007/BF00751335.

Wagner D, Neuhäuser R. 2019. Variation of the auroral oval size and offset for different magnetic activity levels described by the Kp-index. *Astron Nachr* **340(6)**: 483–493. https://doi.org/10.1002/asna.201913601.

Winningham JD, Heikkila WJ. 1974. Polar cap auroral electron fluxes observed with Isis 1. *J Geophys Res (1896–1977)* **79(7)**: 949–957. https://doi.org/10.1029/JA079i007p00949.

Wissing JM, Bornebusch J, Kallenrode M-B. 2008. Variation of energetic particle precipitation with local magnetic time. *Adv Space Res* **41**: 1274–1278. https://doi.org/10.1016/j.asr.2007.05.063.

Wissing JM, Kallenrode M-B. 2009. Atmospheric Ionization Module Osnabrück (AIMOS): A 3-D model to determine atmospheric ionization by energetic charged particles from different populations. *J Geophys Res Space Phys* **114(A6)**: A06104. https://doi.org/10.1029/2008JA013884.

Yakovchuk O, Wissing J. 2019. Magnetic local time asymmetries in precipitating electron and proton populations with and without substorm activity. *Ann Geophys* **37(6)**: 1063–1077. https://doi.org/10.5194/angeo-37-1063-2019.

Yando K, Millan RM, Green JC, Evans DS. 2011. A Monte Carlo simulation of the NOAA POES medium energy proton and electron detector instrument. *J Geophys Res Space Phys* **116(A10)**: A10231.https://doi.org/10.1029/2011JA016671.

Yeager DM, Frank LA. 1976. Low-energy electron intensities at large distances over the Earth's polar cap. *J Geophys Res (1896–1977)* **81 (22)**: 3966–3976. https://doi.org/10.1029/JA081i022p03966.

Zhang Y, Paxton L. 2008. An empirical Kp-dependent global auroral model based on TIMED/GUVI FUV data. *J Atmos Sol Terr Phys* **70(8)**: 1231–1242. https://doi.org/10.1016/j.jastp.2008.03.008.

Cite this article as: Yakovchuk O & Wissing JM 2023. Polar particle flux distribution and its spatial extent. *J. Space Weather Space Clim.* **13**, 9. https://doi.org/10.1051/swsc/2023009.